Swelling capacity of mixed talc-like/stevensite layers in white/green clay infillings ("deweylite"/"garnierite") from serpentine veins of faulted peridotites, New Caledonia

Lionel Fonteneau, Laurent Caner, Sabine Petit, Farid Juillot, Florian Ploquin, Emmanuel Fritsch

Swelling capacity of mixed talc-like/stevensite layers in white/green clay infillings ('deweylite'/'garnierite') found in serpentine veins of faulted peridotites (New Caledonia)

REVISION 2

Lionel FONTENEAU [1], Laurent CANER [2*], Sabine PETIT [2], Farid JUILLOT [3], Florian PLOQUIN [3], Emmanuel FRITSCH [3]

[1]Corescan Pty Ltd, 1/127 Grandstand Road, 6104 Ascot, WA, Australia

[2] Université de Poitiers, Institut de Chimie des Milieux et Matériaux de Poitiers, IC2MP UMR 7285 CNRS, *5 rue Albert Turpain, TSA51106*, 86073 Poitiers cedex 9, France

* Corresponding author, e-mail: laurent.caner@univ-poitiers.fr

[3] Institut de Minéralogie, de Physique des Matériaux et de Cosmochimie (IMPMC), Sorbonne Universités – Université Pierre et Marie Curie UPMC, UMR CNRS 7590, Museum National d'Histoire Naturelle, UMR IRD 206, 101 Promenade Roger Laroque, Anse Vata, 98848, Nouméa, New Caledonia

Abstract: White (Mg-rich) and green (Ni-rich) clay infillings ('deweylite'/'garnierite') found in serpentine veins of faulted peridotite formations from New Caledonia consist of an intimate mixture of fine-grained and poorly ordered 1:1 and 2:1 layer silicates, commonly referred to as non-expandable serpentine-like (SL) and talc-like (TL) minerals. New data on the swelling and shrinking capacity of these layer silicates were gathered from X-ray diffraction (XRD) after saturation of the clay fractions with different cations (Ca^{2+}, Li^{+}, K^{+}), ethylene glycol (EG) solvation, and heating treatments. Simultaneously, layer charge distribution and vacancy density respectively were investigated by FTIR spectroscopy on NH_4-saturated clay fractions

and by XRD on Li-saturated clay fractions before and after heating (Hofmann Klemen treatment). Five clay infillings, with dominant 2:1 layer silicates and variable Ni contents, were selected for this study, from a large set of veinlets, according to their swelling capacity. The crystal chemistry of these samples was established from FTIR spectroscopy and bulk chemical analyses.

The swelling ability of the clay infillings is attributed to the 2:1 layer silicates. It does not seem to be affected by the relative fraction of Mg and Ni in their octahedral sheets. On XRD patterns, the swelling ability is linked to a slight shift of the basal reflection of the 2:1 layer silicates towards low angles for bulk samples and to a split of that reflection in two contributions for clay fractions saturated with Ca (or Li) and solvated with EG. The amplitude of the split increases with the swelling capacity of the sample. It originates mainly from octahedral-layer charge generated by vacant sites. Such results lead us to consider the 2:1 layer silicates of the infillings as an intimate mixture of non-expandable (TL) and expandable (stevensite) phases. In agreement with previous studies which suggested a contribution of hydrothermal processes in the alteration of serpentine species into 2:1 layer silicates, we propose that the proportion of expandable phases in the clay infillings (or vacant sites in the octahedral sheets of the 2:1 layer silicates) could be used as an efficient probe for assessing their temperature of formation. Clay infillings mostly made of stevensite would have formed at ambient temperatures, whereas those consisting mainly of non-expandable TL would have formed at higher temperatures.

Introduction

Nickeliferous laterites developed on ultramafic rocks (e.g. dunite, harzburgite) in tropical regions are of particular interest as they commonly contain two kinds of Ni-silicate ores: (1) ‘clay silicate’ ores, and (2) ‘hydrous Mg/Ni silicate’ ores (Brand et al., 1998; Gleeson et al.,

2004; Freyssinet et al., 2005; Wells et al., 2009, Fritsch et al. 2016). Layer silicates of the 'clay silicate' ores are mostly composed of swelling dioctahedral 2:1 layer silicates (smectite) such as Fe-nontronite, Fe-montmorillonite, and Al-beidellite (e.g. Gaudin et al., 2004). They usually occur in saprolite, at the bottom of thick and poorly drained lateritic profiles developed on ultramafic rocks and correspond to low-grade Ni-deposits (less than 4 wt % Ni). By contrast, layer silicates of the 'hydrous Mg/Ni silicate' ores mostly consist of weakly expandable trioctahedral 1:1 and 2:1 layer silicates of the serpentine (unit cell formula: $Si_2[Mg,Ni]_3O_5(OH)_4$) and talc (unit cell formula: $Si_4[Mg,Ni]_3O_{10}(OH)_2$) mineral groups (e.g. Brindley and Hang, 1973; Brindley and Wan, 1979, Brindley, 1980; Manceau and Calas, 1985; Tauler et al., 2009; Wells et al., 2009). Because of their small size and low crystal order (stacking defects and vacancies), these layer silicates are commonly referred to as serpentine-like (SL) and talc-like (TL) minerals (Villanova-de-Benavent et al., 2014; 2019; Fritsch et al., 2016). Because of similar ionic charge and ionic radius, Ni (0.69 Å) can replace Mg (0.72 Å) in the octahedral sites of trioctahedral clay minerals leading to various mineral series with large ranges in chemical composition (Faust, 1966, Faust and Murata, 1953, Brindley et al., 1977). Mineral associations of trioctahedral 1:1 and 2:1 clay minerals in veinlets are termed deweylite for the white Mg-rich phases (Bish and Brindley, 1978) and garnierite for the bluish green Ni-rich phases (Pecora et al., 1949). Kerolite is the magnesium-rich end-member, while pimelite is the nickeliferous end-member for the TL mineral series. Such layer silicates are present at depth in white (deweylite) to green (garnierite) clay infillings of faulted saprock and observed in both freely and poorly drained lateritic profiles (Cluzel, 2006; Cluzel and Vigier 2008; Fritsch et al., 2016; 2019; Villanova-de-Benavent et al., 2014). They are widely observed in peridotite massifs of New Caledonia and are related to high-grade Ni-deposits (up to 32 wt % Ni).

The two kinds of silicate ores are therefore associated with contrasting geochemical and structural environments, which suggest that they might have formed under distinct weathering (or alteration) conditions. Whereas the 'clay silicate' ores are commonly associated with the vertical development of thick lateritic profiles under poorly drained conditions (e.g. Gaudin et al., 2004), recent studies in New Caledonia suggest that the 'hydrous Mg/Ni layer silicate' ores might have formed in reactivated faults from the hydrothermal alteration of serpentine species into TL minerals during the dismantling and cooling of the ophiolite nappe (Fritsch et al., 2016; 2019; Cathelineau et al., 2017). Hydrous Mg/Ni layer silicates were described elsewhere in different climatic environments but in similar geological settings, for example in serpentinite at structural contacts in Greece (Christidis and Mitsis, 2006) and in Italy (Capitani and Ventruti, 2018).

Detailed textural and mineralogical investigations on the serpentinised and mineralised faults show that minerals of the serpentine group are predominant at the margin of the veins, whereas those of the talc group prevail in association with quartz in their central part (Christidis and Mitsis, 2006; Fritsch et al., 2016, 2019). In addition, TL minerals have locally been described in association with stevensite (Brindley and Hang, 1973, Wiéwióra et al., 1982) or as mixed layers stevensite-talc (Eberl et al., 1982; Christidis and Mitsis, 2006). Stevensite is considered a swelling trioctahedral (Mg, Ni) 2:1 layer silicate (smectite) with a chemical composition similar to that reported for TL minerals but with vacant sites in its octahedral sheets (Christidis and Mitsis, 2006). Scarcely reported worldwide, this swelling phase has most likely been overlooked in recent mineralogical studies on Ni-laterite deposits (Villanova-de-Benavent et al., 2014; 2016; 2019; Fritsch et al., 2016; 2019; Cathelineau et al., 2016; Capitani and Ventruti, 2017; Tauler et al., 2017; Munoz et al., 2019).

This paper describes, for the first time, the occurrence of stevensite in vein-infillings of reactivated faults from peridotitic formations of New Caledonia. Five samples of white

(deweylite) and bluish green (garnierite) clay infillings, with distinct swelling abilities, were selected from a large set of vein infillings to investigate the relationship between swelling capacity, crystal-chemistry, charge deficiency, and structural disorder (stacking defects and vacancies). Our results aim at deciphering the mechanisms involved in these changes of swelling and crystallographic properties in order to better understand the conditions of formation of the hydrous Mg/Ni layer silicates.

Materials and Methods

The five samples investigated in this study (Figures 1 and 2) belong to a large set of clay infillings, whose texture, mineralogy and chemistry were established in previous works (Fritsch et al. 2016, 2019). They were collected at depth in the saprock, more specifically, in fractures of highly serpentinised zones of two peridotite formations (mainly harzburgite) of the New Caledonian mainland (Figure 1): (i) the Koniambo klippe (mining site “Manguen”) on the Western coast (MG1aWill, MG3aWill) and (ii) the Poro klippe (mining site “La Française” of the CFTMC) on the Eastern coast (BONBR2a, BONBR2c, LFSTA5a2). Both klippes are known for an abundance of fractures and associated crosscutting mineralised veins (also named box-works or “Minerai quadrillé” in the French literature), which grade from white (deweylite) to bluish green (garnierite) according to the relative proportion of Mg and Ni. The five samples selected for this study belong to an ultimate episode of clay infillings predominantly made of 2:1 layer silicates (see Fritsch et al. 2016 for a more detailed description of the vein-infillings). They were selected according to their ability to swell and shrink. Shrinking in the field leads to the development of cracks along the clay infillings after exposure of the mining cuts to air (Figure 2b). On thin sections it is also related to the

124 occurrence of a dense network of cracks, more specifically in Ni-rich bands of the infillings
125 (Figure 2d).
126 Samples were air-dried and crushed with a pestle and mortar before chemical and
127 mineralogical investigations. Chemical analyses of the samples were carried out by digestion
128 of 1000 mg of the finely powdered sample in a high-pressure TFM Teflon vessel using an
129 ETHOS 1600 MILESTONE microwave system, with samples digested using a mixture of
130 3mL of HCl (37%), 2mL of HNO_3 (65%), 1.5mL of HF (40%) and 5mL of H_3BO_3 (5%).
131 After digestion the solution was diluted with osmosed water. Si, Mg, Ni, Co, Al, Fe, Ca, Cr
132 and Cu concentrations were determined using a Perkin Elmer 1100b atomic absorption
133 spectrophotometer. Loss on ignition (LOI) was determined after heating at 1000ºC without
134 pre-drying at 105ºC.
135 To determine the clay (<2 μm fraction) mineralogy, bulk samples were gently ground in agate
136 mortar and sieved at 50 μm. The < 50μm fractions were dispersed into 1 mol L^{-1} NaCl and by
137 ultrasonication. This procedure was reproduced five times to ensure complete Na saturation
138 and dispersion of the samples. The clay fractions were then obtained by centrifugation
139 according to the Stokes'law. The suspended clay fractions were flocculated with 0.5 mol. L^{-1}
140 $CaCl_2$ and divided into aliquots for saturation with different cations (Ca^{2+}, K^+, Li^+ and NH_4^+).
141 The aliquots were treated five times with 0.5 mol. L^{-1} $CaCl_2$, and 1 mol. L^{-1} KCl, LiCl, and
142 NH_4Cl, and washed with osmosed water to remove excess salts until a negative test with 1 M
143 $AgNO_3$ was obtained. As Li^+ and NH_4^+ may enhance dispersion and formation of gels, the Li-
144 and NH_4-saturated samples were washed in ethanol instead of osmosed water and ultra-
145 centrifuged (30000 g). K-saturated samples were heated at 20, 150, 350 and 550°C and
146 examined by XRD. Ca-saturated and Li-saturated samples were analysed by XRD both in an
147 air-dried (AD) state and after ethylene glycol solvation (EG, vapour at 50ºC overnight) to
148 assess the swelling capacity of the layer silicates. The Hofmann-Klemen (HK) treatment

149 (Hofmann and Klemen, 1950; Greene Kelly, 1953, 1955) was also applied to the five clay
150 samples to reveal the possible occurrence of octahedral vacancies in clay minerals. The Li-
151 saturated samples were heated overnight at 300°C to induce migration of Li^+ into octahedral
152 vacancies of the phyllosilicates. For trioctahedral smectites the swelling behaviour of the
153 layers after HK treatment depends on the location of the charge. When the charge originates
154 from the octahedral sheet, the Li saturation and heating implies only partial neutralisation of
155 the charge by migration of a monovalent cation (Li^+) in the octahedral vacancy, and the layers
156 may remain expandable in EG (Petit et al., 2008, Gaudin et al., 2004) or glycerol (Brindley
157 and Brown, 1980). Oriented clay mounts were obtained by dropping a small amount of clay
158 suspensions onto glass slides (or zero background Si wafers) and drying them at room
159 temperature. For some preparations the suspensions were made in ethanol to avoid the
160 formation of gels.
161 Bulk mineralogy of samples was determined by XRD on randomly oriented powders in the
162 step scan mode in the range 2–65° 2θ with steps of 0.025° 2θ and a counting time of 229s per
163 step using a Bruker D8 Advance diffractometer (Cu Kα radiation, 40kV and 40mA) equipped
164 with a Lynx eye detector. XRD patterns of oriented preparations were recorded in both AD
165 and EG solvated states in the step scan mode in the range 2–35° 2θ with steps of 0.016° 2θ
166 and a counting time of 229s. Background stripping was carried out on XRD patterns of
167 oriented preparations and the *00l* diffraction peaks of the layer silicates were decomposed into
168 Gaussian curves with Fityk® (Wojdyr, 2010) to determine peak positions, peak areas, and full
169 width at half maximum (FWHM), the latter being converted into coherent scattering domain
170 sizes (CSDS) in the *c* direction (defined by the statistical range of number of layers: *N*).
171 Fourier transform infrared (FTIR) spectra of bulk and <2µm samples were recorded in the
172 middle IR 400-4000 cm^{-1} range (MIR) using a Nicolet 760 FTIR spectrometer in transmission
173 mode with a 4 cm^{-1} resolution. The spectrometer was continuously purged with dry, CO_2-

depleted air. MIR spectra were recorded from disks prepared by mixing 1 mg of the sample with 150 mg of KBr and pressing them at 10 tons.cm^{-2}. Pellets were heated overnight at 110°C to remove absorbed water before the FTIR spectra were recorded. Layer charge distribution, (i.e. tetrahedral (Te), octahedral (Oc) and variable charges), was estimated by quantifying the amount of NH_4^+ fixed by the samples, before and after Li-saturation and heating at 300°C, using the integrated intensity of the υ_4NH_4 band at 1400 cm^{-1} of normalised FTIR spectra (Petit et al., 1998, 2002, 2008; Gaudin et al., 2004, Mano et al., 2014). The NH_4^+ fixed by the swelling layers of the raw samples corresponds to the total charge of the layers (permanent [Te + Oc] + variable edge charges). It is considered as the CEC at the pH of the NH_4Cl solution. After Li saturation and heating at 300°C (HK test), the amount of NH_4^+ fixed by the layer silicates corresponded to the remaining charge, not neutralised by migration of Li^+ in the octahedral sites (Petit et al., 1998, 2006). FTIR spectra of the NH_4^+-saturated samples (NH_4^+ and $Li_{300}NH_4^+$) were recorded using the same amount of clay and normalised to the OH vibration bands of the main SiO band around 1020 cm^{-1}.

Near infrared (NIR) spectra were recorded at a resolution of 4 cm^{-1} from 4000 to 10,000 cm^{-1} in a glass vial, with a Thermo Scientific Integrating Sphere (diffuse reflectance) with an internal InGaAs detector coupled to a Thermo Scientific Nicolet 6700 FT-IR spectrometer.

RESULTS

Mineralogy and crystal-chemistry

Mineralogy and crystal-chemistry of hydrous Mg/Ni layer silicates from the five samples selected for this study were established from XRD (Figures 3, 6 and 9), FTIR spectroscopy (Figure 4, Table 2), and bulk chemical analyses (Table 1, Figure 5). XRD patterns and FTIR

199 spectra are stacked in the figures according to the ability of the samples to swell (the less
200 expandable at the bottom and the more expandable at the top).
201
202 *Bulk mineralogy*
203 In agreement with previous studies carried out on a larger set of mineralised veins (Fritsch et
204 al. 2016), powder XRD patterns of bulk samples (Figure 3) show that the clay infillings of the
205 samples consist of a mixture of 7 Å-type (1:1) layer silicates of the serpentine mineral group
206 (peaks at 7.32 to 7.38 Å and 3.64 to 3.66 Å) and 10 Å-type (2:1) layer silicates of the talc
207 mineral group (peaks at 10.01 to 11.12 Å and at 3.20 to 3.22 Å). The powder XRD pattern of
208 the less expandable sample (MG1aWill) also displays quartz (Qz). According to XRD results,
209 sample BONBR2c, which is free of Ni (white color), is the richest in SL components and
210 contains TL minerals with poorly resolved *001* reflection. Conversely, powder XRD patterns
211 of samples with greater Ni contents (bluish green colours) present better resolved *001*
212 reflection for TL minerals and smaller proportions of serpentine. The position at ~ 1.525 Å
213 for the shared 06-33 reflection of 1:1 and 2:1 layer silicates indicates that all samples consist
214 of pure tri-octahedral clay minerals with a dominance of bivalent cations (Mg^{2+} and Ni^{2+}) in
215 the octahedral sheets (Table 1, Figure 3).
216 The broad basal *001* reflections and the presence of two-dimensional hk bands (20-13) attest
217 to small coherent scattering domain sizes (CSDS), and structural disorder (stacking defects
218 and vacancies) that enable to refer the layer silicates to serpentine-like (SL) and talc-like (TL)
219 minerals (Brindley and Hang, 1973; Brindley et al., 1977; Bish and Brindley, 1978; Brindley
220 and Brown, 1980; Decarreau et al., 1987; Proenza et al. 2008; Tauler et al., 2009; Villanova-
221 de-Benavent et al., 2014; Fritsch et al. 2016). On the powder XRD patterns of the less
222 expandable (MG1aWill) and the most expandable (BONBR2c) samples, the sharp reflection
223 at ~ 2.51 Å (and to a lesser extent that at ~ 2.45 Å) is superimposed to the broad 20-13 band

(Figure 3). These sharp reflections, on broader reflections of cryptocrystalline SL and TL, suggest additional occurrence of crystalline serpentine (Srp) as reported by Fritsch et al. (2016) on XRD patterns (reflection at 2.51 Å for lizardite 1T and 2.45 Å for chrysotile 2M) and on HR-TEM images (large platelets of lizardite and tubular shaped chrysotile). These variations are also consistent with the presence of a peak asymmetry on the low-angle side of the basal reflections. For the most expandable sample (BONBR2c), the first basal reflection of the 7 Å layer silicates was fitted with two Gaussians (not shown): (i) a first one with a narrow reflection at 7.32 Å (CSDS: 60-75 *N*) which is attributed to well-crystallised serpentine residues (Srp) and (ii) a second wide one at 7.38 Å with smaller CSDS (15 *N*) corresponding to poorly ordered SL species (Fritsch et al., 2016). The statistical range of the number of layers (N) can vary widely for the 1:1 layer silicates (from 75 to 15), according to the amount of serpentine residues (Srp) in the samples. By contrast, the CSDS value is systematically smaller for the 10 Å-type layer silicates ($8 < N < 18$), thereby underlining the small size of the poorly crystallized TL minerals.

Mg and Ni speciation in the layer silicates

FTIR spectra (Figure 4) confirm the mineral composition of the samples (mostly made of TL and SL minerals) and reveal the distribution of divalent cations (Mg and Ni) in the octahedral sites of the layer silicates (Farmer, 1974; Gerard and Herbillon, 1983; Balan et al., 2002; Petit, 2005; Christidis and Mitsis, 2006; Jagannadha Reddy et al., 2009; Mano et al., 2014; Baron and Petit, 2016; Baron et al., 2016). In the white and Ni-free clay sample (BONBR2c), the 3697 cm^{-1} and 3650 cm^{-1} bands of the MIR spectrum belong to serpentine species (Figure 4a). They were assigned respectively to the inner OH stretching and the out-of-phase vibrations of the inner-surface OH of lizardite (Balan et al. 2002). On the same spectrum, the band at 3677 cm^{-1} can be assigned to OH stretching vibrations in νMg_3OH configuration of

TL (e.g. Baron et al. 2016). These assignments imply that the bands observed at 7239 cm^{-1} and 7185 cm^{-1} on the NIR spectrum of BONBR2c correspond to second overtone vibrations ($2\nu Mg_3OH$) in SL and TL minerals, respectively. The other bands reported at lower frequencies on the MIR and NIR spectra of the four bluish green clay samples (BONBR2A, MG3aWil, LFSTA5a2 and MG1aWil) most likely result from additional occurrence and distinct distribution of Ni in octahedral sheets of these layers silicates. More specifically, the 3628 cm^{-1} (MIR – Figure 4a) and 7081 cm^{-1} (NIR – Figure 4b) bands are respectively assigned to first and second overtones Ni_3OH stretching for TL minerals and trioctahedral smectites (Farmer, 1974; Gerard and Herbillon, 1983; Petit, 2005; Christidis and Mitsis, 2006; Jagannadha Reddy et al., 2009; Mano et al., 2014; Baron and Petit, 2016; Baron et al., 2016). The 3650 cm^{-1} (MIR – Figure 4a) and 7125 cm^{-1} (NIR – Figure 4b) bands can also be attributed to first and second overtones $MgNi_2OH$ stretching for TL minerals (Petit et al., 2004; Baron and Petit, 2016). As highlighted by Fritsch et al. (2019), these results suggest that TL minerals (and/or trioctahedral smectite) are the main Ni-bearing phases of the Ni-silicate ores. Nevertheless, the bands at 3650 cm^{-1} (MIR) and 7125 cm^{-1} (NIR) could also be assigned to νNi_3OH in serpentine (Baron et al., 2016). These bands are commonly poorly resolved, except for sample MG1aWill, which could therefore contain Ni-rich SL minerals (Nepouite) in addition to Ni-rich TL minerals (Pimelite).

Chemical composition

Bulk chemical compositions of the five samples (expressed in oxide weight %) are listed in table 1. These layer silicates are mainly composed of Si with minor Fe, highly variable Mg, and Ni contents (or reverse Mg and Ni variations), and are free of Al. Bulk chemical data converted to number of atoms and plotted in a ternary Si/(Mg+Fe)/Ni diagram (Figure 5) reveal that all five samples are within a triangle delineated by the Mg/Fe end-member of

serpentine species (Srp), and the Mg and Ni end-members of talc (Tlc). As outlined by Fristch et al. (2016; 2019), the relative proportion of TL minerals in mixtures of both 7 Å and 10 Å layer silicates can be assessed from the mole Si:ΣR ratio (with ΣR = Mg+Fe+Ni). This ratio is shown on the ternary diagram by a horizontal line. Theoretically, it ranges from 2/3 in samples composed exclusively of serpentine species [$R_3Si_2O_5(OH)_4.nH_2O$] to 4/3 in those composed only of 2:1 layer silicates in the talc mineral group [$R_3Si_4O_{10}(OH)_2$] (see the two horizontal solid lines in Figure 5). The ternary Si/(Mg+Fe)/Ni diagram shows, therefore, that the five samples present dominant TL minerals in the mixture of 7 Å and 10 Å layer silicates, which is consistent with Si:ΣR ratios greater than 1.00. This is consistent with XRD patterns showing a major contribution of the basal reflections of the 2:1 layer silicates compared to those of the 1:1 layer silicates (Figure 3). Samples with the highest Si/ΣR ratios and lowest Fe contents (Table 1) are predominantly made of TL minerals and are, therefore, the closest to the theoretical line for talc on the ternary diagram. This is the case for samples MG1aWill and MG3aWill. The presence of quartz in MG1aWill, in addition to TL minerals, as highlighted by XRD, may also increase the Si/ΣR and thus induce an overestimation of the proportion of TL minerals. Major chemical changes are related to a right shift of the data from the Mg+Fe pole to the Ni pole of the ternary diagram. In agreement with our IR data, this shift points to a gradual increase of the Ni for Mg substitution in the layer silicates (mostly TL minerals) of the infillings. This substitution rate is nil in the most expandable sample (BONBR2c) and optimal in the less expandable sample (MG1aWill).

Swelling and shrinking behaviour

XRD patterns of oriented mounts of the < 2 μm fraction of the five samples saturated with Ca or Li in AD and EG states are given in Figure 6. XRD patterns of the Ca-saturated samples in AD state are very similar to the XRD patterns of the powder bulk samples (Figure 3). They all

299 present similar peak position and broadening of the basal *00l* reflections characteristic of
300 poorly crystalline 1:1 (SL) and 2:1 (TL) layer silicates. The position of the *001* reflection of
301 the 2:1 layer silicates in AD state ranges from 9.92 Å (MG1aWill) to 10.20 Å (BONBR2c)
302 for the Ca-saturated samples (Figure 6a, Table 2) and from 9.92 Å (MG1aWill) to 10.82 Å
303 (BONBR2c) for the Li-saturated samples (Figure 6b, Table 2). The position of this reflection
304 at about 10 Å is slightly greater than that generally reported at 9.6 Å for non-expandable TL
305 minerals (Brindley et al., 1977).
306 XRD patterns of the Ca or Li-saturated samples in EG state (Figure 6) show no significant
307 change of peak position for the 1:1 layer silicates (Srp and SL), indicating an absence of
308 swelling phase (Figure 6). The *001* reflection of the 2:1 layer silicates for MG1aWill is at the
309 same position (~ 10 Å) in the AD and EG states confirming also the absence of swelling
310 phase (Figures 6 and 7; Table 2). The most expandable sample (BONBR2c) exhibits a *001*
311 peak of 16.47 Å for CaEG and 17.04 Å for LiEG, and a *002* peak of ~ 8.80-8.90 Å for CaEG
312 and LiEG (Figures 6 and 7; Table 2). These harmonic peaks are close to that reported by
313 Christidis and Mitsis (2006) for stevensite (respectively 17.6 Å and ~ 9.02 Å). The other
314 samples have intermediate amounts of expandable and non-expandable layers, according to
315 the position of the first basal reflection between 10 and 17 Å in EG state. Figures 6a and 6b
316 also show that EG solvation of the two most expandable samples, BONBR2a and BONBR2c,
317 saturated with Li^+ leads to greater resolution of reflections, as well as to a greater shift of the
318 peaks towards low angles (i.e. larger d-spacing) than for samples saturated with Ca (Table 2).
319 Such differences likely result from the smaller size of Li^+ and different ionic potential
320 compared to Ca^{2+}, implying different solvation behaviours with water or ethylene glycol.
321 The swelling and the splitting of the *001* reflection in samples BONBR2a, BONBR2c and
322 MG3aWill are better illustrated in background stripped patterns (Figure 7). The asymmetric
323 *001* reflection at ~10.0 Å for the 2:1 layer silicates in AD state (dots in Figure 7) can be fitted

with two overlapping Gaussian curves (dashed lines, Figure 7). The peak asymmetry disappears with EG solvation and is replaced by two contributions, which are fitted with two separate Gaussian curves (plain line). From bottom to top of Figure 7, the increase of the swelling ability of the three samples is linked to a shift of the first contribution (P1) towards low angles (14.15 Å for MG3aWill, 15.27 Å for BONBR2c and 17.04 Å for BONBR2a) with a concomitant increase of the peak area. On the opposite, the second contribution (P2) shift towards greater angles (9.44 Å for MG3aWill, 9.24 Å for BONBR2c and 8.83 Å for BONBR2a) and gradually collapse. These variations suggest therefore a random interstratification (R0) between swelling (smectite) and non-swelling phases (TL) with a variable proportion of the two components.

Figure 8 displays the positions of both contributions (P1 and P2) for the five Ca- and Li-saturated samples in EG state. The progressive variation of the P1 and P2 positions from samples MG1aWill to BONBR2c suggests a continuum between the non-expandable TL and the fully expandable smectite. It also shows that the P1 and P2 positions are negatively correlated and that non-expandable TL minerals and stevensite are present at the extremities of the trend. More specifically, P1 and P2 are merged and located close to the *001* reflection of the non-expandable TL minerals (corresponding to a d-spacing of ~ 9.6 Å) in the non-swelling sample (MG1aWill) and widely dissociated and positioned close to the *001* (P1) and *002* (P2) reflections of stevensite (d-spacing close to 17.6 Å and 8.8 Å, respectively) in the highly swelling sample (BONBR2c). Accordingly, the position of both reflections (P1 and P2) could be used to assess the relative proportion of swelling layers (stevensite) in the pool of the 2:1 layer silicates.

Following K-saturation and gradual heating from room temperature to 550°C, the *001* reflection of TL was displaced from 10.0-9.9 Å to 9.6-9.7 Å (Figure 9). Simultaneously, the intensity and width of the d_{001} peaks, as well as the asymmetry on the low angle side,

decreased with increasing heating for all samples except MG3aWILL. These variations indicate a preferential collapse of the swelling (or hydrated) layers of these clay minerals. The position of the *001* reflection at ~9.6 Å after heating and the destruction of the swelling layers therefore reveals the non-expandable TL minerals (Brindley et al., 1977). At 550 °C the collapse of the *001* reflection is complete for serpentine (thermal dehydroxylation of Srp and SL minerals) whereas it remains partial for TL minerals.

Layer charge and vacancies

XRD patterns of the Li-saturated samples after heating at 300°C (Hofmann Klemen treatment) show a peak displacement from 10.87 Å (LiAD) to 10.44 Å (Li_{300}) for BONBR2c and from 10.07 Å (LiAD) to 9.93 Å (Li_{300}) for MG1aWill (Li_{300}, Figure 6b). For the five samples the intensity of collapse is related to the proportion of swelling layers. Following EG solvation after HK treatment (Li_{300EG} Figure 6b) the 001 and 002 peaks are broad and hardly discernible from the background for samples BONBR2a, BONBR2c and LFSTA5a2, and their position ranges from ~15 Å to ~ 17 Å and from ~ 9.4 Å to ~ 8.8 Å, respectively. This behaviour indicates that the layer charge is partially neutralised by migration of Li^+ ions toward vacant sites upon HK treatment, and thus that it originates from the octahedral sheet.

The comparison of the FTIR NH_4 band before and after the HK treatment (i.e. NH_4^+-saturated samples previously saturated with Li and heated at 300°C: $Li_{300}NH_4$) reveals a charge loss that ranges from 63% in the highly expandable sample (BONBR2c) to 39% in the non-expandable one (MG1aWill; Table 3). Upon Li-saturation the samples with the highest swelling ability show the largest charge loss, whereas those with the lowest swelling capacity show the lowest loss of charge neutralised by Li^+. The swelling ability is thus correlated with the amount of charge neutralised by Li^+ and hence with the amount of octahedral vacancies. The swelling components of these samples can thus be identified as trioctahedral 2:1 layers

374 with octahedral vacancies, and therefore as stevensite layers. The decreasing of swelling
375 ability after HK treatment indicates a loss of layer charge due to partial neutralisation of the
376 charge of the stevensite by Li^+ after heating. This is consistent with what is expected for
377 trioctahedral smectites with octahedral charge where Li-saturation followed by heating (HK
378 treatment) induces partial neutralisation of approximately half of the charge (Li^+ vs. R^{2+}; Petit
379 et al., 2008).
380

381 **DISCUSSION AND CONCLUSIONS**

382

383 **Swelling capacity and octahedral vacancies of hydrous Mg/Ni layer silicates**

384

385 The hydrous Mg/Ni layer silicates found in clay infillings of faulted peridotites have recently
386 been related to the early alteration of serpentine veins and conversion of serpentine species
387 into cryptocrystalline SL residues and newly formed TL minerals (Fritsch et al., 2016). These
388 tri-octahedral layer silicates of the serpentine and talc mineral groups have often been
389 considered as non-expandable and the occurrence of swelling layers (i.e. stevensite) has
390 scarcely been reported worldwide (Christidis and Mitsis, 2006; Capitani and Ventruti, 2018).
391 Our work suggests that such occurrence could be more systematic than initially considered. It
392 links the swelling capacity of the samples to the content of stevensite layers (or octahedral
393 vacancies) in the pool of the 2:1 layer silicates of the clay infillings, using XRD and FTIR
394 investigations on clay saturated samples (Ca^{2+}, Li^+, NH_4^+, K^+) submitted or not to ethylene
395 glycol and heating treatments.
396 Swelling of the 2:1 layer silicates is related on XRD patterns of Ca- or Li-saturated and air-
397 dried clay samples to a shift towards low angles of their *001* basal reflection (or development
398 of a peak asymmetry or shoulder on the low angle slopping side of that reflection), and to a

399 split of this reflection in two contributions (P1 and P2) after solvation of the saturated clay
400 samples with ethylene glycol. The amplitude of the split increases with the swelling capacity
401 of the samples. It is nil (P1 = P2) in samples composed of non-expandable TL minerals (*001*
402 peak close to 9.6 Å) and optimal in samples composed exclusively of stevensite within the
403 pool of the 2:1 layer silicates, (P1: *001* peak at ~ 17.0 Å, P2: *002* peak at ~ 8.8). Intermediate
404 values for P1 and P2 between these two poles (Figure 8), together with considerable peak
405 width and irrational basal reflections point to the presence of random interstratification (R0)
406 between non-expandable TL and expandable stevensite. These intermediate values could also
407 be due to three-component mixed layers (Figure 10) including non-expandable TL layers,
408 partially expanded stevensite (one sheet of EG), and fully expanded stevensite (two sheets of
409 EG) (Eberl et al., 1982; Christidis and Eberl, 2003).
410 In this study we also closely linked the swelling behaviour of the clay infillings to layer
411 charge and octahedral vacancies in the 2:1 layer silicates (Hofman Klemen test). As illustrated
412 on figure 10, larger d-spacings (or hydration) in stevensite layers originate from larger
413 numbers of vacant sites in the octahedral sheets and divalent cations (Mg^{2+}, Ni^{2+}) in the
414 interlayer spaces. The non-expandable layers with a low charge are assigned to TL (unit cell
415 formula: $Si_4[Mg, Ni]_3O_{10}(OH)_2$, nH_2O); Figure 10a). Conversely, the fully expandable layers
416 with higher charge and optimum octahedral vacancies are assigned to stevensite (unit cell
417 formula: $(Mg^{2+},Ni^{2+})_xSi_4[Mg, Ni]_{3-x}\square_xO_{10}(OH)_2$ nH_2O with $\square$ being a random vacancy;
418 Figure 10 b and c). In stevensite, a fraction of divalent cations (Mg^{2+} and Ni^{2+}) no longer
419 occupy octahedral sites, but inter-layer positions (exchangeable cation). Petit et al. (2008)
420 showed for synthetic Zn-stevensite that layers having a charge < ~0.2 (per half unit cell) are
421 non-expandable while layer having a charge > ~0.2 (per half unit cell) can swell upon
422 ethylene glycol solvation.

423 The proportion of Ni in the octahedral sheets of the 2:1 layer silicates (or Ni for Mg
424 substitution rate) does not seems to affect the swelling capacity of these minerals. Although
425 the richest Ni-sample (MG1aWill) contains only non-expandable TL and the Ni-free sample
426 (BONBR2c) mostly stevensite in the pool of the 2:1 layer silicates, the relationship between
427 the Ni for Mg substitution rate and swelling capacity of the 2:1 layer silicates is not as
428 obvious with the other samples (BONBR2A, MG3aWil, LFSTA5a2). On the other hand,
429 Fritsch et al. (2019) reported an opposite trend based on the relationship established on thin
430 sections between the Ni content and anisotropy of the TL infillings. Indeed Mg-rich domains
431 in these clay infillings (kerolite) are commonly anisotrope and observed as botryoidal-shaped
432 ribbons, whereas Ni-rich domains of the same infillings (pimelite) are optically isotrope and
433 cryptocrystalline. This suggests greater amounts of crystal defects (including octahedral
434 vacancies) in pimelite (Ni-rich) compared to kerolite (Mg-rich), which is supported on thin
435 sections by the larger development of cracks in the Ni-rich parts (or bands) of the TL
436 infillings (Figure 2d). Accordingly, further investigation should be undertaken on a larger set
437 of clay infillings to better establish the relationships between Ni for Mg substitution and
438 vacancies in TL minerals.
439
440 ***Conditions of formation***
441 Recent mineralogical and chemical studies on the white and green clay infillings
442 (deweylite/garnierite) found at depth (saprock) in reactivated faults of peridotite formations
443 from New Caledonia have suggested the contribution of temperature and pressure (i.e.
444 hydrothermal processes) in the alteration of serpentine veins into clay infillings
445 predominantly made of TL minerals (Fritsch et al., 2016, 2019; Cathelineau et al., 2017).
446 More precisely, Fritsch et al. (2019) emphasised that temperature in the clay infillings could
447 have affected the size and crystallinity of the 2:1 layer silicates that we assign in this work to

448 TL minerals, interstratified TL/stevensite and stevensite. On the other hand, laboratory
449 experiments carried out by Decarreau et al. (1987) have shown that the stability fields of talc,
450 kerolite and Mg or Ni-stevensite are temperature-dependent. Stevensites can be synthesised
451 below 100°C, kerolites between 100 and 170°C, and talc at higher temperatures (above
452 500°C). We conclude then that the proportion of stevensite (or vacant sites) in the pool of the
453 2:1 layer silicates could be used as an efficient probe for assessing their temperature of
454 formation. Vein infillings exclusively composed of non-expandable TL as 2:1 layer silicates
455 would have precipitated well above 100°C, whereas those composed of almost pure stevensite
456 would have formed below that temperature (i.e. closer to ambient temperature). This
457 interpretation suggests that temperature could have controlled the distribution of non-
458 expandable TL and expandable stevensite along reactivated faults during the early alteration
459 of the peridotite formations. Both mineral phases would have precipitated simultaneously but
460 at different places along the fault network. However, stevensite could also have been
461 produced later during the interaction of meteoric fluids with faulted peridotites and the
462 development of thick lateritic profiles by weathering and hydration of TL minerals into poorly
463 ordered and highly swelling smectite.
464
465 **Some possible technological implications**
466
467 Nickel is widely used in industry, because of its chemical and physical properties and
468 resistance to corrosion, for the production of stainless steel, alloys and plating (~70% of Ni
469 consumption), for the production of electric batteries (~30% of Ni consumption), and to a
470 lesser extent as a catalyst. The demand for Ni increases at a rate of ~4 % per year and it will
471 continue to rise in the near future with the development of electrical vehicle/batteries. Nickel
472 is mainly exploited from sulphide and lateritic ores which respectively correspond to 30-40%

and 60-70% of the world resource (Schnebele, 2017). Sulphide ores with high Ni grades have been the dominant source of Ni because processing is simple and cheaper than for laterites. In the recent years, the proportion of Ni extracted from sulphide ores gradually decreased (currently 60-65% of Ni production) with the rarefaction of these deposits (Bergmann, 2003; Gleeson, et al., 2003; Dalvi et al., 2004; Butt and Cluzel, 2013), while that of lateritic ore increased (currently 35-40% of Ni production) and will continue to rise. Because of the progressive decrease in the Ni grade of available laterite ores, the environmental issues, and to help the economically co-exploitation of associated trace metals (e.g. Co in limonitic ores), industrial processes of Ni extraction are becoming more and more complex. Pyrometallurgical processes are predominant for sulphides but the use of hydrometallurgical processes, such as Acid Leaching (AL) or High-Pressure Acid Leaching (HPAL) is increasing for both sulphide and laterite ores (Diaz et al., 1998, McDonald and Whittington, 2008; Rice, 2016; Ucyildiz and Girgin, 2017, Mano et al., 2019). These processes work better for low-grade ores and have better Ni, and other metal, recoveries. To improve these processes, detailed knowledge of the actual mineralogy and crystal-chemistry of Ni-bearing clay silicates is becoming more and more mandatory for economically viable (Ni recovery) and environmentally sustainable (acid consumption) Ni mining.

There is also an increasing interest in the use of Ni-bearing phyllosilicates as catalysts because Ni is one of the most active metals for the dry reforming of methane (activation of C-H bond) and the cleavage of C-C bonds (Wang et al., 1998; Vogels et al., 2005; Iwasa et al. 2006; Sivaiah et al., 2010; Yoshida et al. 2015; Akri et al., 2017). These Ni-clays can be natural or easily synthesised (Iwasa et al. 2006, Baron et al., 2016). The Ni-based catalysts are reduced to between 500 and 800 °C to produce active metal Ni. The Ni content of the Ni-phyllosilicates, their crystal-chemistry (octahedral vs. exchangeable Ni) and resistance to temperature are key parameters in the catalytic efficiency.

ACKNOWLEDGEMENTS

The authors thank Fabien Trotet, Pierre Epinoux, Philippe Bains, Philippe Hoffler, Gilles Monteil (SLN), Julie Michaud (SMT/SMCB), Yann Dijkstra, René Feré (CFTMC), Clément Couteau, Frédéric Villedieu (KNS) and Christian Tessarolo (Goro-VALE) who provided helpful technical reports and assistance for access to mining sites. The authors gratefully acknowledge the associate editor, and the two reviewers, G. Christidis and an anonymous reviewer, for their constructive comments, which allowed significant improvement of the manuscript. This research was funded by the projects “Conditions of formation of Mg/Ni silicate ores from New Caledonia” (2010, INSU CESSUR) and “Ni/Co mineralisation factors of laterites derived from ultramafic rocks of New-Caledonia” (2010-2014, CNRT Nickel and its environment). The authors acknowledge financial support from the European Union (ERDF) and "Région Nouvelle Aquitaine".

REFERENCES

Akri M., Pronier S., Chafik T., Achak O., Granger P., Simon P., Trentesaux M. and Batiot-Dupeyrat C. (2017) Development of nickel supported La and Ce-natural illite clay for autothermal dry reforming of methane: Toward a better resistance to deactivation. Applied Catalysis B: Environmental, 205, 519–531

Balan, E., Saitta, A.M., Mauri, F., Lemaire, C. and Guyot, F. (2002) First-principles calculation of the infrared spectrum of lizardite. American Mineralogist, 87, 1286–1290.

521 Baron, F., Pushparaj, S.S.C., Fontaine, C., Sivaiah, M.V., Decarreau, A., Petit, S. (2016)
522 Microwave-assisted hydrothermal synthesis of Ni-Mg layered silicate clays. Current
523 Microwave Chemistry, 3, 85–89.
524 Baron, F. and Petit, S. (2016) Interpretation of the infrared spectra of the lizardite-nepouite
525 series in the near-and mid-infrared range. American Mineralogist, 101, 423–430.
526 Bergman, R.A. (2003) Nickel Production from Low-Iron Laterite ores: process Description.
527 CIM Bulletin, 96, 127–138.
528 Bish D. L. and Brindley G. W. (1978) Deweylites, mixtures of poorly crystalline hydrous
529 serpentine and talc-like minerals. Mineralogical Magazine, 42, 75–79.
530 Brand, N.W., Butt, C.R.M. and Elias, M. (1998) Nickel laterites: classification and features.
531 AGSO Journal of Australian Geology and Geophysics, 17, 81–88.
532 Brindley, G.W. (1980): The structure and chemistry of Hydrous Nickel-containing silicate
533 and Nickel-Aluminium Hydroxy minerals. Bulletin de Minéralogie, 103, 161–169.
534 Brindley G.W. and Hang P. T. (1973) The nature of garnierites-I: Structures, chemical
535 compositions and color characteristics. Clays and clays minerals, 21, 27–40.
536 Brindley G.W., Bish D. L. and Wan H. M. (1977) The nature of kerolite, its relation to talc
537 and stevensite. Mineralogical magazine, 41, 443–452.
538 Brindley G.W. and Wan H.M. (1979) Compositions, structures, and properties of nickel-
539 containing minerals in the kerolite-pimelite series. American Mineralogist, 64, 615–625.
540 Brindley G.W. and Brown, G. (1980) Crystal structures of clay minerals and their X-ray
541 identification. Mineralogical society, London, 494 p.
542 Butt C.R.M. and Cluzel D. (2013) Nickel Laterite Ore Deposits: Weathered Serpentinites.
543 Elements, 9, 123–128

544 Capitani, G.C. and Ventruti, G. (2018) Ni-serpentine nanoflakes in the garnierite ore from
545 Campello Monti (Strona Valley, Italy): Népouite with some pecoraite outlines and the
546 processing of Ni-containing ore bodies. American Mineralogist, 103, 629–644.
547 Cathelineau, M., Myagkiy, A., Quesnel, B., Boiron, M.C., Gautier, P., Boulvais, P., Ulrich,
548 M., Truche, L., Golfier, F., Drouillet, M. (2017) Multistage crack seal vein and
549 hydrothermal Ni enrichment in serpentinised ultramafic rocks (Koniambo massif, New
550 Caledonia). Mineral. Depos., 52, 961–978.
551 Christidis G. E. and Mitsis I. (2006) A New Ni-rich stevensite from the ophiolite complex of
552 Othrys, central Greece. Clays and Clay Minerals, 54, 653–666.
553 Cluzel D., 2006. Synthèse géologique de la Nouvelle-Calédonie et de sa zone économique
554 exclusive. Rapport de synthèse de la convention ISTO-IFREMER, programme
555 EXTRAPLAC.
556 Cluzel, D. and Vigier, B. (2008) Syntectonic mobility of supergene nickel ores from New
557 Caledonia (Southwest Pacific). Evidences from faulted regolith and garnierite veins.
558 Resource Geology, 58, 161–170.
559 Dalvi, A., Bacon, G. and Osborne, R. (2004) The past and the future of nickel laterites. In:
560 PDAC 2004 International convention, Toronto, Canada. Trade show and investors
561 exchange. Toronto: Prospectors and Developers Association of Canada, 7–10.
562 Decarreau, A., Colin, F., Herbillon, A., Manceau, A., Nahon, D., Paquet, H., Trauth-Badaud,
563 D., and Trescases, J. J. (1987) Domain segregation in Ni-Fe-Mg-smectites: Clays and
564 Clay Minerals, 35, 1–10.
565 Diaz, M.C., Landolt, C.A., Vahed, A., Warner, A.E.M. and Taylor, J.C. (1988) A review of
566 nickel pyrometallurgical operations. Journal of metals, 40, 9, 28–33.
567 Eberl, D.D. Jones, B.F. and Khoury, H.N. (1982) Mixed-layer kerolite/stevensite from the
568 Amargosa Desert, Nevada. Clays and Clay Minerals, 30, 321–326.

569 Farmer, V.C. (1974) The Infrared Spectra of Minerals, 539 p. The Mineralogical Society,
570 London.
571 Faust, G.T. (1966) The hydrous nickel-magnesium silicates - The garnierite group. American
572 Mineralogist, 51, 279–298.
573 Faust G.T. and Murata K.J. (1953) Stevensite, redefined as a member of the montmorillonite
574 group. American Mineralogist, 38, 973–987.
575 Freyssinet, P., Butt, C.R.M., Morris, R.C. and Piantone, P. (2005) Ore-forming processes
576 related to lateritic weathering. In: Hedenquist JW, Thomson JFH, Goldfarb RJ, Richards
577 JP (eds), Economic Geology 100th Anniversary Volume. Economic Geology Publishing
578 Company, New Haven, Connecticut, 681–722.
579 Fritsch, E., Juillot, F., Dublet, G., Fonteneau, L., Fandeur, D., Martin, E., Caner, L., Auzende,
580 A.L., Grauby, O. and Beaufort. D. (2016) An alternative model for the formation of
581 hydrous Mg/Ni layer silicates (‘deweylite’/‘garnierite’) in faulted peridotites of New
582 Caledonia: I. Texture and mineralogy of a paragenetic succession of silicate infillings.
583 European Journal of Mineralogy, 28, 295–311.
584 Fritsch, E.J.C., Juillot, F., Dublet, G., Fonteneau, L., Fandeur, D., Martin, E., Caner, L.,
585 Auzende, A.L. and Beaufort. D. (2019) An alternative model for the formation of
586 hydrous Mg/Ni layer silicates (“deweylite”/“garnierite”) in faulted peridotites of New
587 Caledonia: II. Petrography and chemistry of white and green clay infillings. European
588 Journal of Mineralogy, 31, 945–962.
589 Gaudin A., Grauby O., Noack N., Decarreau A. and Petit S. (2004) Accurate crystal chemistry
590 of ferric smectites from the lateritic nickel ore of Murrin Murrin (Western Australia). I.
591 XRD and multi-scale chemical approaches. Clay Minerals, 39, 301–315.
592 Gerard P. and Herbillon A.J. (1983) Infrared studies of Ni-bearing clay minerals of the
593 kerolite-pimelite series. Clays and Clays minerals, 31, 143–151.

Gleeson S.A., Butt C.M.R. and Elias M. (2003) Nickel laterites: a review. SEG Newsletter, Society of Economic Geology, 54, 9–16.

Gleeson, S.A., Herrington, R.J., Durango, J., Velasquez, A. an Koll, G. (2004) The Mineralogy and Geochemistry of the Cerro Matoso S.A. Ni Laterite Deposit, Montelibano, Colombia. Economic Geology, 99, 1197–1213.

Greene-Kelly, R. (1953) Irreversible dehydration in montmorillonite. Part II. Clay Minerals Bulletin. 1, 52–56.

Greene-Kelly, R. (1955) Dehydration of montmorillonite minerals. Mineralogical Magazine, 30, 604–615.

Hofmann, U. and Klemen, R. (1950) Verlust der austausehfahigkeit von lithiumionen an Bentonit durch Erhitzung. Zeitschrift für Anorganische und Chemie, 262, 95–99.

Iwasa N., Takizawa M. and Arai M. (2006) Preparation and application of nickel-containing smectite-type clay materials for methane reforming with carbon dioxide. Applied Catalysis A: General, 314, 32–39

Jagannadha Reddy, B., Frost, R. L. and Dickfos, M. J. (2009) Characterisation of Ni silicate bearing minerals by UV–vis–NIR spectroscopy - Effect of Ni substitution in hydrous Ni–Mg silicates. Spectrochimica Acta, Part A, 1762–1768.

Manceau A. and Calas G. (1985) Heterogeneous distribution of nickel in hydrous silicates from New Caledonia ore deposits. American Mineralogist, 70, 549–558.

Mano, E.S., Caner, L., Petit, S., Chaves, A.P. and Mexias, A.S. (2014) Mineralogical characterisation of Ni-bearing smectites from Niquelândia, Brazil. Clays and Clay Minerals, 62, 324–335.

Mano, E.S., Caner, L., Petit, S., Chaves A. P. and Mexias, A.S. (2019) Ni-smectitic ore behaviour during the Caron Process. Hydrometallurgy, 186, 200–209.

618 McDonald R.G. and Whittington B.I. (2008) Atmospheric acid leaching of nickel laterites
619 review Part I. Sulphuric acid technologies. Hydrometallurgy, 91, 35–55.
620 Pecora W.T., Hobbs S.W. and Muraxa K.J. (1949) Variations in garnierite from the nickel
621 deposit near Riddle, Oregon. Economic Geology, 44, 13–23.
622 Petit, S. (2005) Crystal-chemistry of talcs: a NIR and MIR spectroscopic approach. In: J.T.
623 Kloprogge, (Ed.), The Application of Vibrational Spectroscopy to Clay Minerals and
624 Layered Double Hydroxides: CMS Workshop Lectures, Aurora, Colorado. 13, 41–64.
625 Petit, S., Righi, D., Madejová, J. and Decarreau, A. (1998) Layer charge estimation of
626 smectites infrared spectroscopy. Clay Minerals, 33, 579–591.
627 Petit, S., Caillaud, J., Righi D., Madejová, J., Elsass, F. and Köster, H.M. (2002)
628 Characterisation and crystal chemistry of an Fe-rich montmorillonite from Ölberg,
629 Germany. Clay Minerals, 37, 283–297.
630 Petit, S., Martin, F., Wiewióra, A., De Parseval, P. and Decarreau, A. (2004) Crystal-
631 chemistry of talc: a near infrared (NIR) spectroscopy study. American Mineralogist, 89,
632 319–326.
633 Petit, S., Righi, D. and Madejová, J. (2006) Infrared spectroscopy of NH_4^+-bearing and
634 saturated clay minerals: A review of the study of layer charge. Applied Clay Science, 34,
635 22–30.
636 Petit, S., Righi, D. and Decarreau, A. (2008) Transformation of synthetic Zn-stevensite to Zn-
637 talc induced by the Hofmann-Klemen effect. Clays and Clay Minerals, 57, 645–654.
638 Proenza, J.A., Lewis, J.F., Galí, S., Tauler, E., Labrador, M., Melgarejo, J.C., Longo, F.,
639 Bloise, G. (2008): Garnierite mineralisation from Falcondo Ni-laterite deposit
640 (Dominican Republic). Macla, 9, 197–198.
641 Rice, N. M. (2016) A hydrochloric acid process for nickeliferous laterites. Minerals
642 Engineering, 88, 28–52.

643 Schnebele E. K. (2017) U.S. Geological Survey, Mineral Commodity Summaries. 206p.

644 Sivaiah, M.V.. Petit, S. Barrault, J. Batiot-Dupeyrat, C. and Valange, S. (2010) CO_2
645 reforming of CH_4 over Ni-containing phyllosilicates as catalyst precursors. Catalysis
646 Today, 157, 397–403.

647 Tauler, E., Proenza, J.A., Galí, S., Lewis, J.F., Labrador, M., García-Romero, E., Suárez, M.,
648 Longo, F., Bloise, G. (2009) Ni-sepiolite-falcondoite in garnierite mineralisation from the
649 Falcondo Ni-laterite deposit, Dominican Republic. Clay Minerals, 44, 435–454.

650 Ucyildiz A. and Girgin I. (2017) High pressure sulphuric acid leaching of lateritic nickel ore.
651 Physicochemical Problems of Mineral Processing, 53, 475−488

652 Villanova-de-Benavent, C., Proenza, J.A., Galí, S., García-Casco, A., Tauler, E., Lewis, J.F.
653 and Longo, F. (2014) Garnierites and garnierites: Texture, mineralogy and geochemistry
654 in the Falcondo Ni-laterite deposit, Dominican Republic. Ore Geology Reviews, 58 C,
655 91–109.

656 Vogels R.J.M.J., Kloprogge J.T. and Geus J.W. (2005) Catalytic activity of synthetic saponite
657 clays: effects of tetrahedral and octahedral composition. Journal of Catalysis, 231, 443-
658 452.

659 Wang S., Zhu H.Y. and Lu G. Q. (1998) Preparation, Characterization, and Catalytic
660 Properties of Clay-Based Nickel Catalysts for Methane Reforming. Journal of Colloid
661 and Interface Science, 204, 128–134

662 Wells, M.A., Ramanaidou, E.R., Verrall, M. and Tessarolo, C. (2009) Mineralogy and crystal
663 chemistry of ‘‘garnierites’’ in the Goro lateritic nickel deposit, New Caledonia. European
664 Journal of Mineralogy, 21, 467–483.

665 Wiéwióra A., Dubinska E. and Iwasinska I. (1982) Mixed-layering in Ni-containing talc-like
666 minerals from Szklary, Lower Silesia, Poland. Proceedings of the International Clay
667 Conference, Pavia, Italy, 111–125.

668 Wojdyr, M. (2010) Fityk: a general-purpose peak fitting program: Journal of Applied
669 Crystallography, 43, 1126-1128.
670 Yoshida H., Watanabe K., Iwasa N., Fujita S. and Arai M. (2015) Selective methanation of
671 CO in H_2-rich gas stream by synthetic nickel-containing smectite based catalysts. Applied
672 Catalysis B: Environmental 162, 93–97
673

Table captions

Table 1: Chemical analyses of the five samples.

Table 2: Peak position (in Å) of the < 2 μm fraction after saturation with Ca or Li in AD and EG states. For EG state the position of the peak at low angle (P1: 4-7 °2θ) and at high angle (P2: 7-10 °2θ) are given.

Table 3: Estimation of the layer charge loss of the samples using NH_4^+ saturation and measurement of the area of the band at 1400 cm^{-1} on MIR spectra before and after Li saturation and heating.

Figure captions

Figure 1: Peridotite formations of New Caledonia and location of the sampling sites for the Mg/Ni silicate ores of the Koniambo and Poro massifs (arrows).

Figure 2: **(a)** General view of reactivated cross-cutting faults with white (Dew: deweylite) and bluish green (Gar: garnierite) coatings (or infillings) along black serpentine network of saprock (SR_{Hz}) of thick Ni-lateritic profiles (Poro, Fatma), **(b)** Close up of **(a)** showing olive green (STL) and turquoise (TL) infillings of a garnierite vein (Gar) with numerous cracks (note also at the periphery of the vein remains of black serpentines and in its central part a thin white silica infilling, Qz), **(c)** Densely cracked turquoise (sample BONBR2a) and white infillings (sample BONBR2c) along serpentine veins (Srp) of hazburgite saprolite (SAP_{Hz}), **(d)** BSE image of a garnierite vein showing the whole sequence of clay (STL, TL) and silica

(Qz) infillings. In this vein, the development of cracks (due to drying) is mostly observed in the Ni-rich (light grey) part of the TL infilling.

Figure 3: XRD patterns of randomly oriented powders of the five samples showing broad diffraction peaks of the serpentine-like (SL – 1:1) and talc-like (TL – 2:1) mineral phases and sharp and smaller peaks for residual serpentine species (Srp: mainly lizardite Lz and chrysotile Ctl) and quartz (Qz).

Figure 4: FTIR spectra of the < 2 µm fractions of the five samples **(a)** in the OH-stretching region (Middle Infrared) and **(b)** in the first OH overtone region (Near Infrared) of the 1:1 and 2:1 layer silicates.

Figure 5: Plot of the molar chemical composition of the five samples selected for this study (arrows) (see also table 1 for the chemical composition of the five samples in oxides wt %) in a ternary Si *vs* Mg+Fe *vs* Ni diagram within the set of samples investigated by Fritsch et al. (2016, 2019) for Mg/Ni layer silicates of the serpentine (Srp) and talc (Tlc) groups from New Caledonia.

Figure 6: XRD patterns of oriented clay preparation of the five samples submitted to Ca saturation (a) and Li saturation (b) in the air-dried (AD) and ethylene glycol solvated (EG) states. Plain line CaAD or LiAD, dashed line: CaEG or LiEG. (b) two additional XRD pattern per sample: dotted line: Li_{300} after heating at 300°C (Hofman Klemen treatment), dash-dotted line: Li_{300}EG after heating at 300°C and solvation with EG.

723

724 **Figure 7**: Decomposition of XRD patterns of Li saturated clay fractions in AD and EG states
725 of the three most expandable samples (MG3aWill, BONBR2a and BONBR2c) in the angular
726 domain 3-13° 2θ after background stripping. Dots: experimental values, plain lines: best fit,
727 dashed lines: elementary Gaussian contributions (in the EG state the Gaussian contribution is
728 identical with the best fit).

729

730 **Figure 8**: Position of the reflection at low angle (P1: 4-7 °2θ) and at high angle (P2: 7-10
731 °2θ) of the 2:1 component in CaEG and LiEG states, determined by XRD decomposition of
732 most swelling samples (MG3aWill, BONBR2a and BONBR2c).

733

734 **Figure 9:** XRD patterns of oriented preparation of the five clay samples saturated with K at
735 room temperature (AD 20°C, plain line) and after heating at 150°C (dashed line), 350°C
736 (doted line) and 550°C (dash-doted line).

737

738 **Figure 10:** Structure of the three components (a-TL, b-partly expanded stevensite and c-fully
739 expanded stevensite) of the interstratified 2:1 layer silicates. The increase of the d-spacing
740 from left to right is closely linked to an increase of vacant sites in the octahedral sheets and
741 hydrated cations (Mg, Ni) in the interlayer spaces.

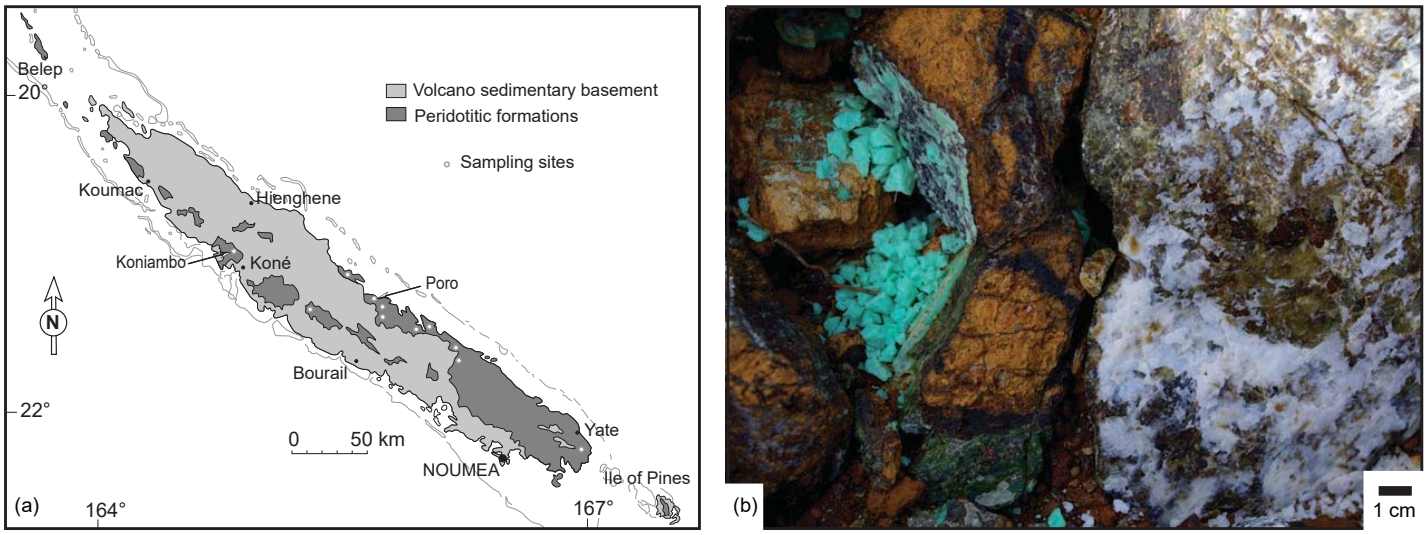
Belep
20°
Volcano sedimentary basement
Peridotitic formations
Sampling sites
Koumac
Hienghene
Koniambo
Koné
Poro
N
Bourail
22°
0
50 km
Yate
NOUMEA
Ile of Pines
(a)
164°
167°
(b)
1 cm

Figure 1

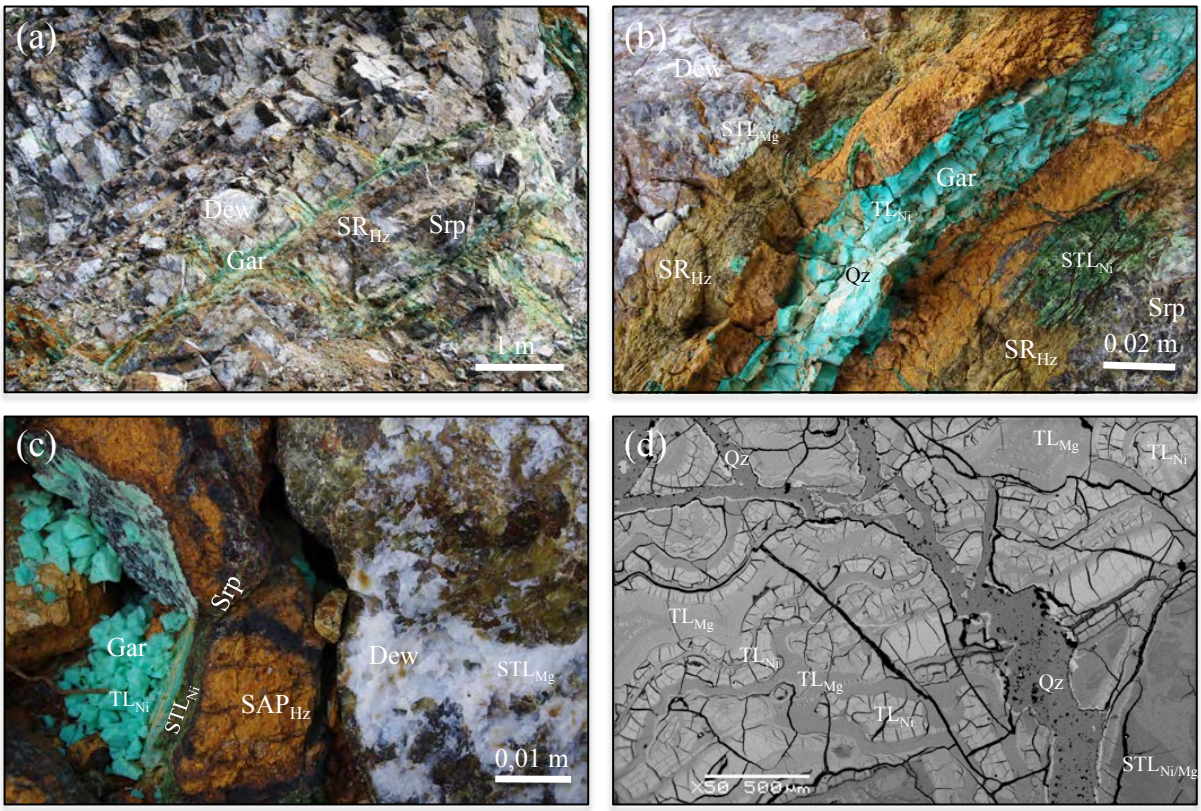
(a)
Dew
SR$_{Hz}$
Srp
Gar
1 m
(b)
Dew
STL$_{Mg}$
Gar
TL$_{Ni}$
SR$_{Hz}$
Qz
STL$_{Ni}$
Srp
SR$_{Hz}$
0.02 m
(c)
Srp
Gar
TL$_{Ni}$
STL$_{Ni}$
SAP$_{Hz}$
Dew
STL$_{Mg}$
0.01 m
(d)
Qz
TL$_{Mg}$
TL$_{Ni}$
TL$_{Mg}$
TL$_{Mg}$
TL$_{Ni}$
TL$_{Mg}$
TL$_{Ni}$
Qz
STL$_{Ni/Mg}$
x50 5000µm

Figure 2

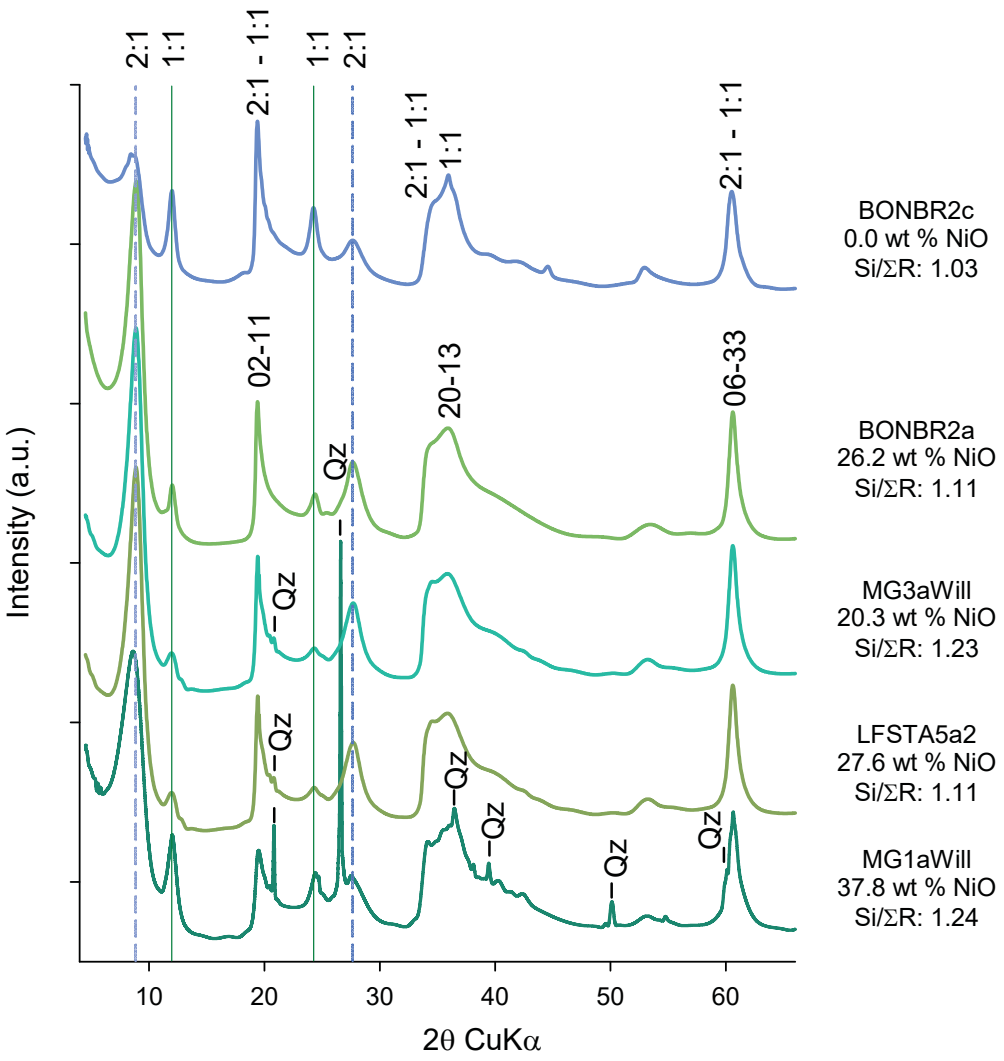
2:1
1:1
2:1 - 1:1
1:1
2:1
2:1 - 1:1
1:1
2:1 - 1:1
02-11
Qz
20-13
06-33
Qz
Qz
Qz
Qz
Qz
Qz
BONBR2c
0.0 wt % NiO
Si/ΣR: 1.03
BONBR2a
26.2 wt % NiO
Si/ΣR: 1.11
MG3aWill
20.3 wt % NiO
Si/ΣR: 1.23
LFSTA5a2
27.6 wt % NiO
Si/ΣR: 1.11
MG1aWill
37.8 wt % NiO
Si/ΣR: 1.24
Intensity (a.u.)
10
20
30
40
50
60
2θ CuKα

Figure 3

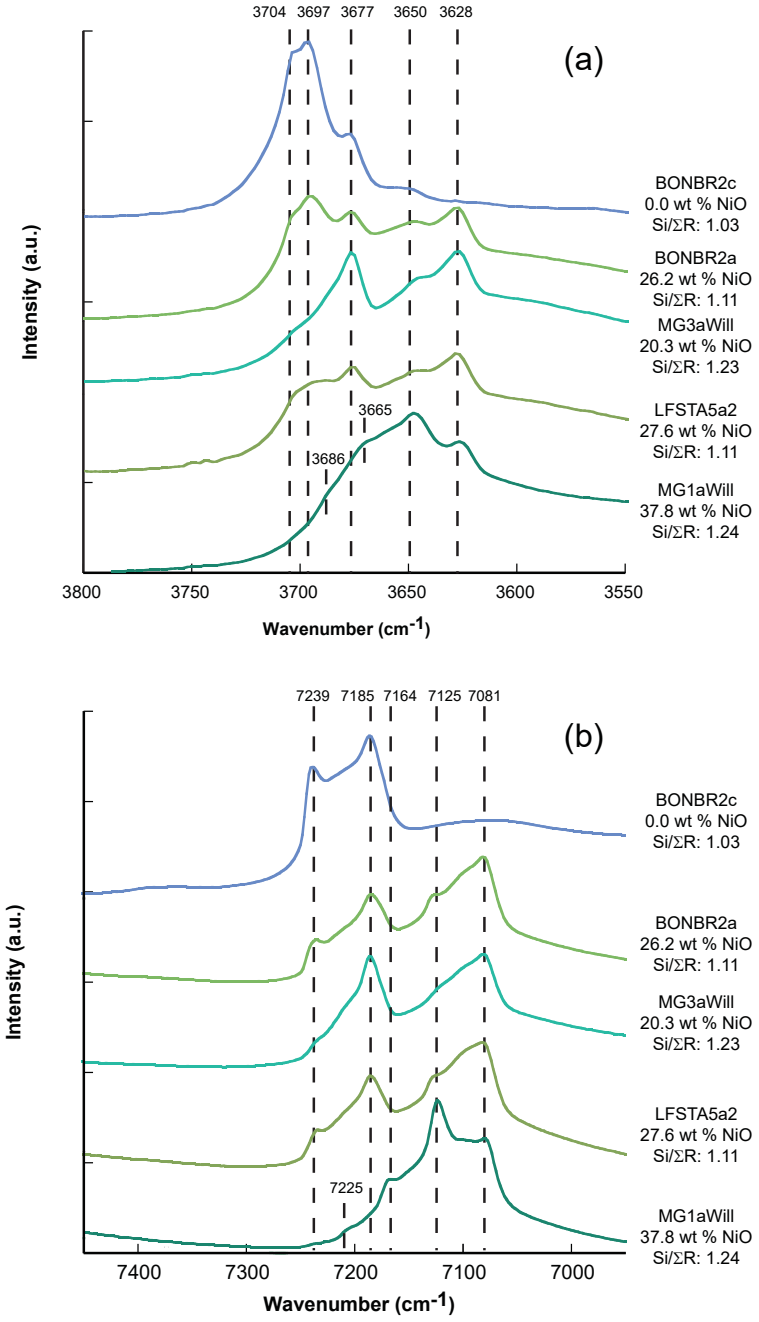
(a)
3704
3697
3677
3650
3628
3665
3686
BONBR2c
0.0 wt % NiO
Si/ΣR: 1.03
BONBR2a
26.2 wt % NiO
Si/ΣR: 1.11
MG3aWill
20.3 wt % NiO
Si/ΣR: 1.23
LFSTA5a2
27.6 wt % NiO
Si/ΣR: 1.11
MG1aWill
37.8 wt % NiO
Si/ΣR: 1.24
Intensity (a.u.)
3800
3750
3700
3650
3600
3550
Wavenumber (cm-1)
(b)
7239
7185
7164
7125
7081
7225
BONBR2c
0.0 wt % NiO
Si/ΣR: 1.03
BONBR2a
26.2 wt % NiO
Si/ΣR: 1.11
MG3aWill
20.3 wt % NiO
Si/ΣR: 1.23
LFSTA5a2
27.6 wt % NiO
Si/ΣR: 1.11
MG1aWill
37.8 wt % NiO
Si/ΣR: 1.24
Intensity (a.u.)
7400
7300
7200
7100
7000
Wavenumber (cm-1)

Figure 4

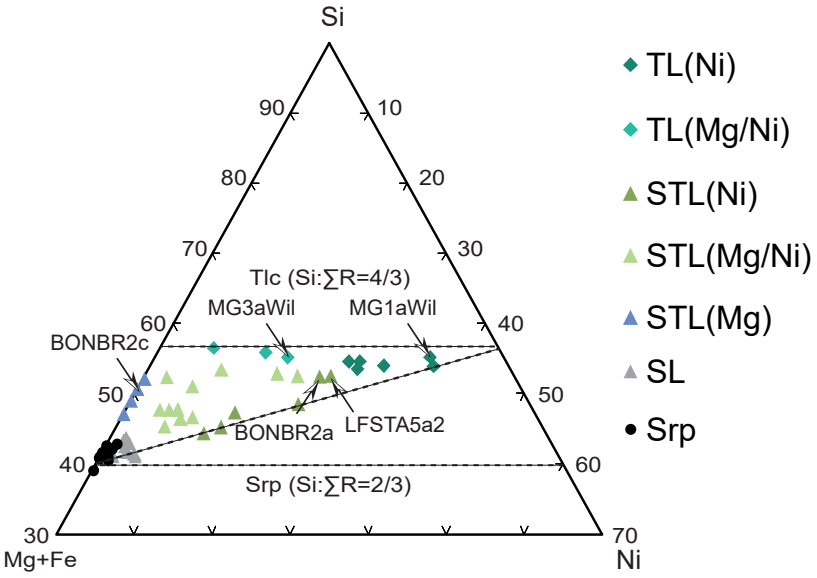
Si
90
10
80
20
70
30
60
40
50
50
40
60
30
70
Mg+Fe
Ni
TIc (Si:∑R=4/3)
MG3aWil
MG1aWil
BONBR2c
BONBR2a
LFSTA5a2
Srp (Si:∑R=2/3)
TL(Ni)
TL(Mg/Ni)
STL(Ni)
STL(Mg/Ni)
STL(Mg)
SL
Srp

Figure 5

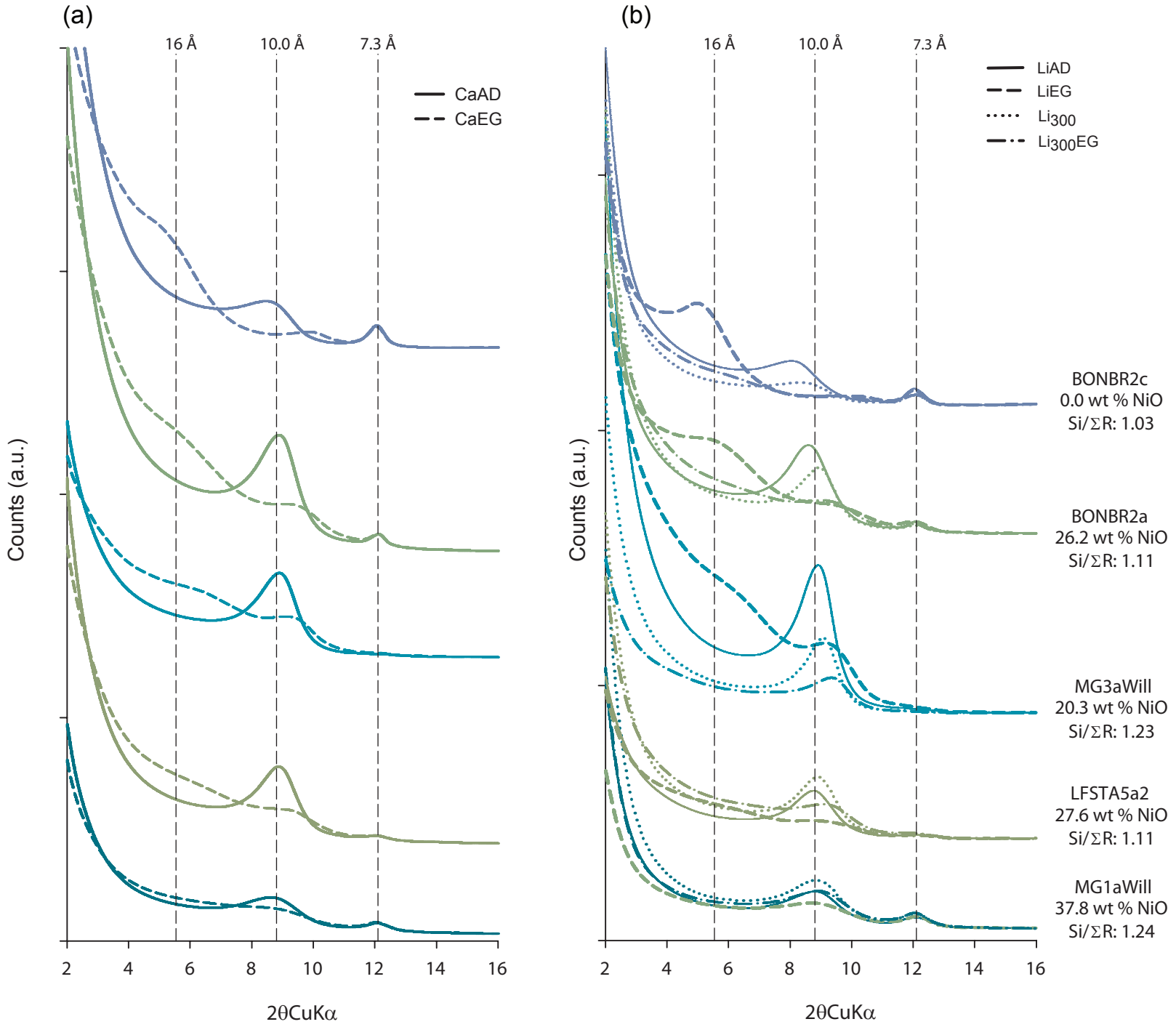
(a)
16 Å
10.0 Å
7.3 Å
CaAD
CaEG
Counts (a.u.)
2θCuKα
(b)
LiAD
LiEG
Li300
Li300EG
BONBR2c
0.0 wt % NiO
Si/ΣR: 1.03
BONBR2a
26.2 wt % NiO
Si/ΣR: 1.11
MG3aWill
20.3 wt % NiO
Si/ΣR: 1.23
LFSTA5a2
27.6 wt % NiO
Si/ΣR: 1.11
MG1aWill
37.8 wt % NiO
Si/ΣR: 1.24

Figure 6

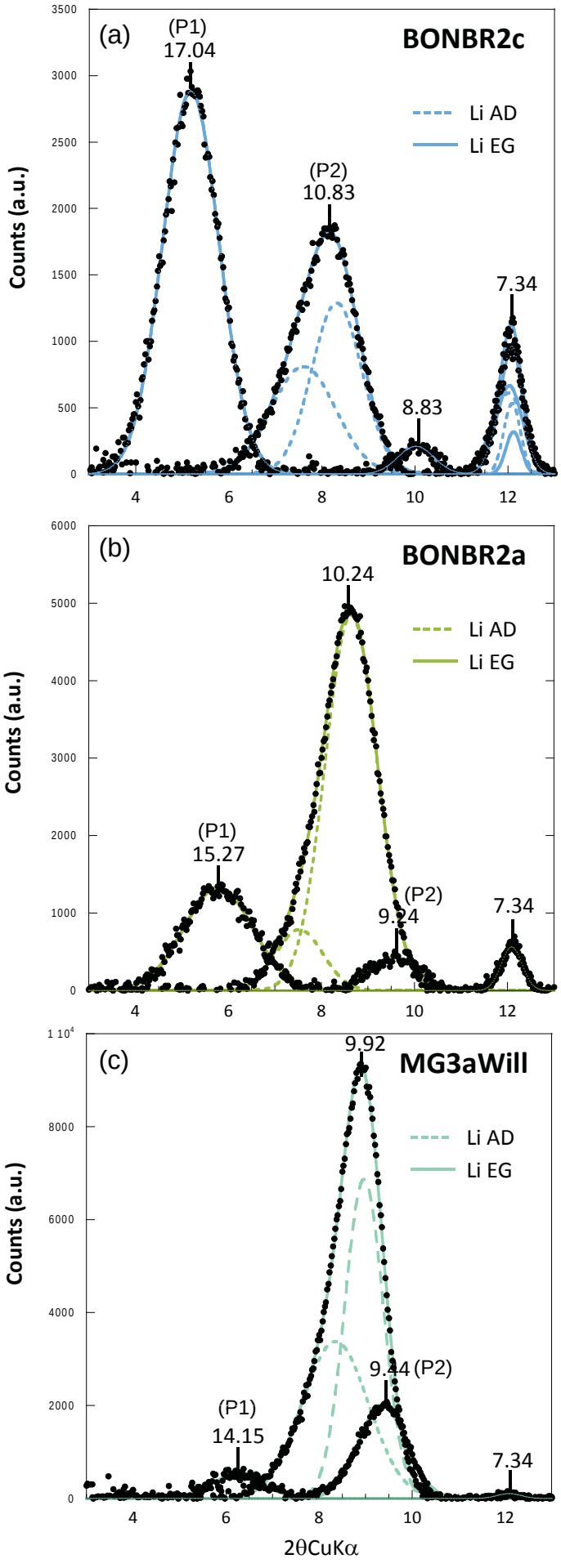
(a)
BONBR2c
(P1)
17.04
(P2)
10.83
8.83
7.34
Li AD
Li EG
Counts (a.u.)
(b)
BONBR2a
10.24
(P1)
15.27
(P2)
9.24
7.34
Li AD
Li EG
Counts (a.u.)
(c)
MG3aWill
9.92
9.44 (P2)
(P1)
14.15
7.34
Li AD
Li EG
Counts (a.u.)
2θCuKα

Figure 7

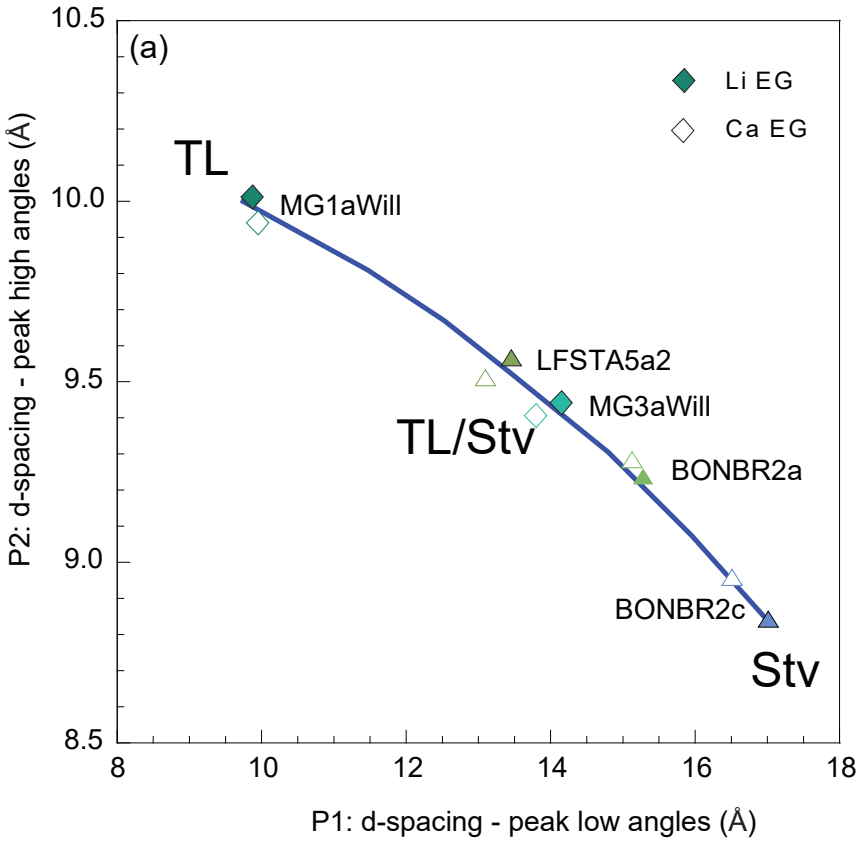
(a)
Li EG
Ca EG
TL
MG1aWill
LFSTA5a2
MG3aWill
TL/Stv
BONBR2a
BONBR2c
Stv
P2: d-spacing - peak high angles (Å)
P1: d-spacing - peak low angles (Å)
10.5
10.0
9.5
9.0
8.5
8
10
12
14
16
18

Figure 8

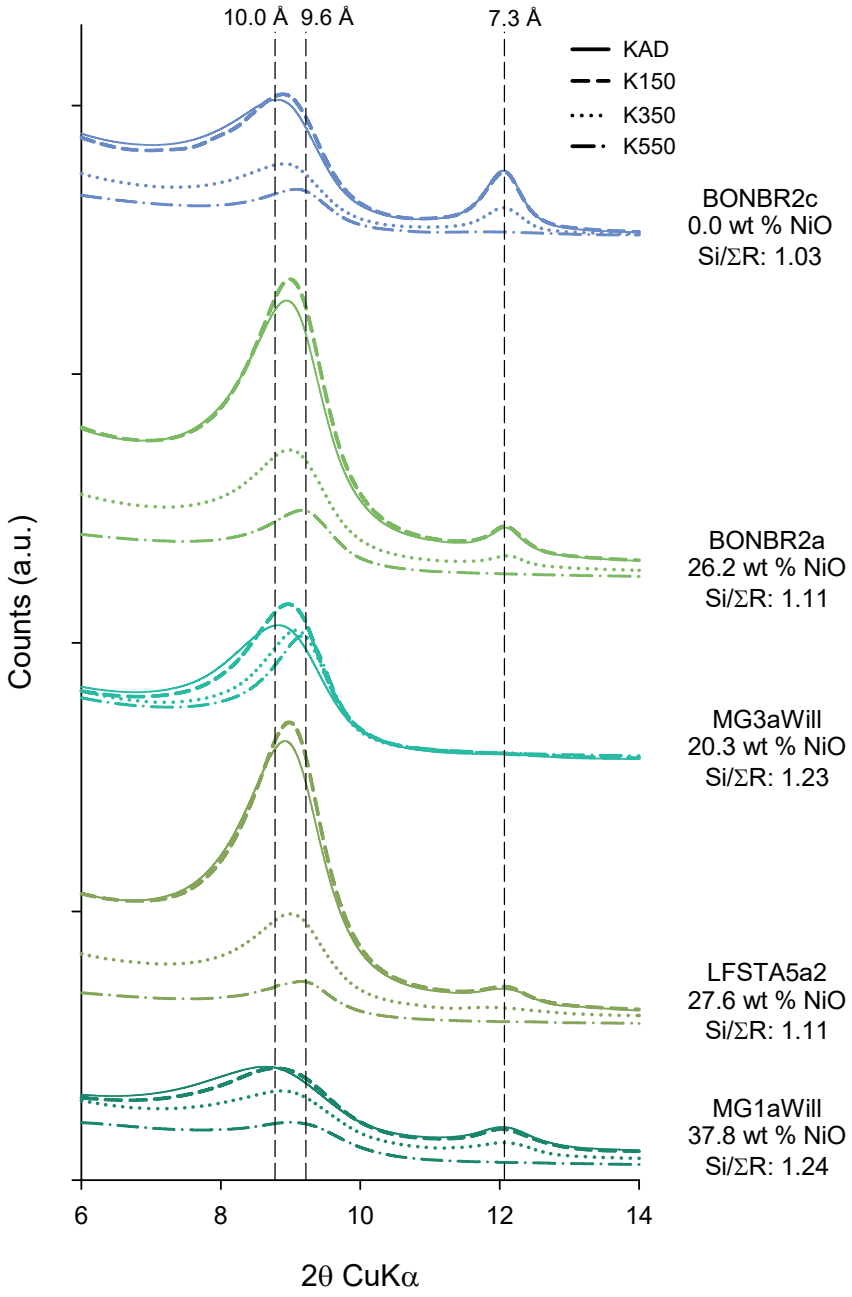
10.0 Å
9.6 Å
7.3 Å
KAD
K150
K350
K550
BONBR2c
0.0 wt % NiO
Si/ΣR: 1.03
BONBR2a
26.2 wt % NiO
Si/ΣR: 1.11
MG3aWill
20.3 wt % NiO
Si/ΣR: 1.23
LFSTA5a2
27.6 wt % NiO
Si/ΣR: 1.11
MG1aWill
37.8 wt % NiO
Si/ΣR: 1.24
Counts (a.u.)
6
8
10
12
14
2θ CuKα

Figure 9

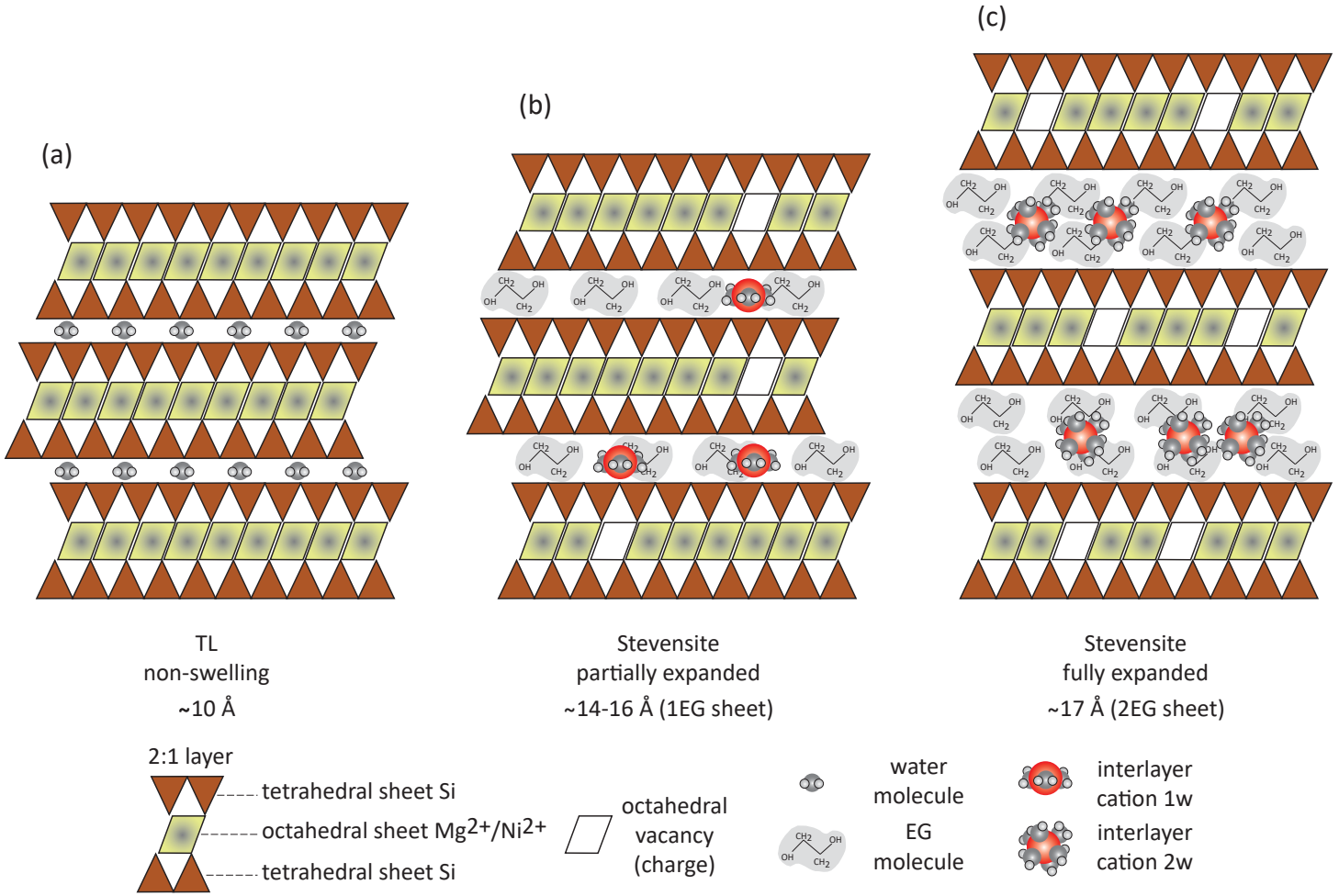
(a)
(b)
(c)
TL
non-swelling
~10 Å
Stevensite
partially expanded
~14-16 Å (1EG sheet)
Stevensite
fully expanded
~17 Å (2EG sheet)
2:1 layer
tetrahedral sheet Si
octahedral sheet Mg2+/Ni2+
tetrahedral sheet Si
octahedral
vacancy
(charge)
water
molecule
EG
molecule
interlayer
cation 1w
interlayer
cation 2w